Relationship between turbulent structures and heat transfer in microfin enhanced surfaces using large eddy simulations and particle image velocimetry

Puxuan Li [a,*], Matthew Campbell [a], Ning Zhang [b], Steven J. Eckels [a]

[a] *Institute for Environmental Research, Department of Mechanical and Nuclear Engineering, Kansas State University, Manhattan, KS 66506, USA*
[b] *Department of Chemical, Civil and Mechanical Engineering, McNeese State University, Lake Charles, LA 70609, USA*

ABSTRACT

Internally enhanced surfaces such as micro-fins are an important class of heat transfer enhancement in commercial applications. Many research papers discuss the design and optima of these surfaces. However, most previous studies have demonstrated only the macro relationship between the geometries of the micro-fins and heat transfer. The need for a deeper understanding of these fins arose from some currently unsolved problems that limit future development of enhanced surfaces. First, why are increases of heat transfer larger than area increases in micro-finned tubes in most cases? Second, why do internally micro-finned tubes typically have lower heat-transfer-enhanced ratios in laminar and transition flows? This work presents a novel method to analyze the detailed relationship between flow characteristics and heat transfer for one type of micro-fin. The goal of the paper was not to find a new Reynolds number-based correlation, but to find flow patterns responsible for heat transfer enhancement and understand the mechanisms that cause this. First, this paper introduces comprehensive experimental measurements including particle image velocimetry (PIV), measurement of the heat transfer coefficient and accuracy of pressure-drop measurements, all used to validate numerical approaches. Validated large eddy simulations (LES) are then used to predict flow characteristics and coherent structures (Q criterion). The numerical simulation includes both heat conduction in the metal structure and heat convection on the solid–fluid interface. Finally, the paper documents how the flow structures link with the enhancement of heat transfer in the micro-finned duct.

1. Introduction

Internally enhanced surfaces such as micro-fins are an important class of heat transfer enhancement in commercial applications such as air conditioners and refrigerators. Micro-fins are characterized by fin structures less than 1 mm in height that are used in ducts and tubes of a significantly larger diameter. One typical goal of micro-fin design is to increase heat transfer with a minimum pressure-drop penalty. It has been generally reported that two key factors lead to the enhancement of heat transfer. These are the area increase and fluid mixing in the inter-fin region caused by flow separation and reattachment [1]. Normally, researchers follow a fixed procedure to analyze the macro relationship between heat transfer and micro-fins: (1) the study identifies a range of geometries of interest, and physical or numerical models

are prepared; (2) then, all collected experimental and numerical results are shown in common plots with heat transfer characteristics (heat transfer coefficient or Nusselt number) versus Reynolds numbers; and (3) finally, physics and mechanics behind the plots are discussed, and correlations are proposed. The correlations reveal how newly designed geometries, i.e., width, height, shape, angle, etc., affect the heat transfer and pressure drops, but are not predictive for new geometries because the detailed flow physics are not identified. Very few studies have explored the link between flow characteristics and heat transfer both experimentally and numerically. The detailed time-resolved characteristics of flow near the wall around the micro-fins are not well understood because experimental and numerical data are limited, which gave rise to some currently unsolved problems. First, in most cases, it is not well understood why increases in heat transfer are larger than area increases in the micro-finned tubes [1–10]. Second, why do internally micro-finned tubes usually have a lower heat-transfer-enhanced ratio in the laminar and transition flow regions [2]? The current study proposes some novel methods of collecting

* Corresponding author at: Institute for Environmental Research, 0056 Seaton Hall, 920 N. 17th St., Manhattan, KS 66506, USA.
E-mail address: puxuanli@ksu.edu (P. Li).

Nomenclature

a	z-intercept		*Greek letters*	
b	slope		β	thermal diffusivity
C_k	coefficient for LDKM		δ	delta function
C_ε	coefficient for LDKM		Δ	local grid scale
dt	time step size		ΔT	temperature difference
e	heat capacity		Δx^+	grid resolution for LES in X direction
$\overrightarrow{F}$	external body forces		Δy^+	grid resolution for LES in Y direction
$\overrightarrow{g}$	gravitational acceleration		∇	vector differential operator
k_{sgs}	subgrid-scale kinetic energy		κ	thermal conductivity
p	pressure		μ_t	subgrid-scale eddy viscosity
q''	heat flux		ν	kinematic viscosity
S	strain-rate tensor		ρ	density
t	time		τ	stress tensor
T	temperature			
u	velocity		*Acronyms and abbreviations*	
u_τ	friction velocity		*HTC*	Heat Transfer Coefficient
u_i'	velocity fluctuation		LDKM	Localized Dynamic Kinetic Energy Subgrid-Scale Model
un	uncertainty of each source		LES	Large Eddy Simulation
U	velocity magnitude		PIV	Particle Image Velocimetry
UN_{HTC}	total uncertainty of *HTC*		RANS	Reynolds Averaged Navier–Stokes equations
X	X-axis		RSM	Reynolds Stress Equation Model
Y	Y-axis		SGS	Subgrid-scale
Z	Z-axis		*TKE*	Turbulent Kinetic Energy
			WMLES	Algebraic Wall-Modeled LES Model

and analyzing the data to figure out the physics and mechanics driving the performance of the micro-finned tubes. The goal of the paper was not to find a new Reynolds number-based correlation but to find flow patterns responsible for heat transfer enhancement and understand the mechanisms that cause it.

In a micro-finned tube, a certain number and shape of protruding micro-fins were extruded or rolled onto the tube wall. For the convenience of collecting experimental data, the primary test section in the current study was a square duct with clear upper and side walls (vapor-polished polycarbonate) on a solid copper block as shown in Fig. 1(a). The fin structure matched one used by Webb et al. [1] and was manufactured on the top of the copper block through micro-machining. Webb chose the height of the fin to be located in the viscous sublayer. The fluid flowing in the duct was water. A commercial, telescopic, particle image velocimetry (PIV) system captured flow characteristics in the duct. PIV is a powerful tool used in many configurations [11–15]. However, it is rarely used to collect flow characteristics near heat transfer fins. Dupuis et al. [16] identified and analyzed flow structures in pyramidal-pin fin arrays for laminar flow. Their fins were sprayed on aluminum substrates with dimensions of 7 mm × 51 mm. Fin height was 1.0 mm, and fin base length was 1.5 mm. In their study, PIV measured not only instantaneous velocity fields but also other related properties such as turbulent intensity. The flow in their study was pure nitrogen. Flow structures obtained in the micro-channel affected flow stability, structure and turbulence level, which contributed to the increase of the convective heat transfer coefficient. In 2017, Xia et al. [17] presented experimental results of the laminar-flow behavior of water in circular micro pin-fin, square micro pin-fin and diamond micro pin-fin heat sinks with PIV. The entire dimension with the micro-pin fin arrays was 10 mm (length) × 2.2 mm (width) × 0.1 mm (height). Vortexes in their study explained why the best heat transfer enhancement behaviors were in the diamond micro pin-fin heat sink. With an increasing Reynolds number, vortexes in the diamond micro pin-

fin occurred the earliest and had the most complicated structure, which effectively improved the mixing of fluid and heat transfer. In the above examples, PIV was applied to micro-channels. For the current study, PIV was used in a larger passage with smaller micro-fins (micro-fin height/duct height ≈ 0.022).

The experimental data also provided an opportunity to validate numerical techniques. Previously, there had been numerous numerical investigations of the micro-fins [16,18–23]. $k - \varepsilon$ turbulence models were used in most of the papers mentioned above. However, two drawbacks existed in the turbulence model. First, the $k - \varepsilon$ turbulence model was not suitable for the laminar and transition flow region of micro-fin flows, which led to faulty predictions of heat transfer and pressure drops [24]. Second, the turbulence model developed from Reynolds Averaged Navier–Stokes equations (RANS) was not able to simulate the dynamic process of fluid mixing caused by flow separation and reattachment within the inter-fin region. By carefully utilizing our validation data, we revealed that a large eddy simulation (LES) with a localized dynamic kinetic energy subgrid-scale model (LDKM) [25] predicted the flow observed with PIV. The authors were aware of only a few systematic studies in the literature on implementing LES in wall-bounded flows with heat transfer in micro-fins. In 2019, Campet et al. [23] presented a LES approach to study the turbulent flow in a single-started helically ribbed tube. Numerical simulations in the paper were conducted in ANSYS Fluent, which comprised the broad physical modeling capabilities needed to model flow and heat transfer. Fluent offers different parallel processing options [26] to increase calculation speeds. In the current study, a stream-wise periodic boundary condition significantly reduced computational time without sacrificing accuracy. In such flow configurations, the geometry varies in a repeating manner along the direction of the flow, leading to a periodic, fully developed flow regime in which the flow pattern repeats in successive cycles [24]. Campet et al. [23] also used the similar periodic boundaries.
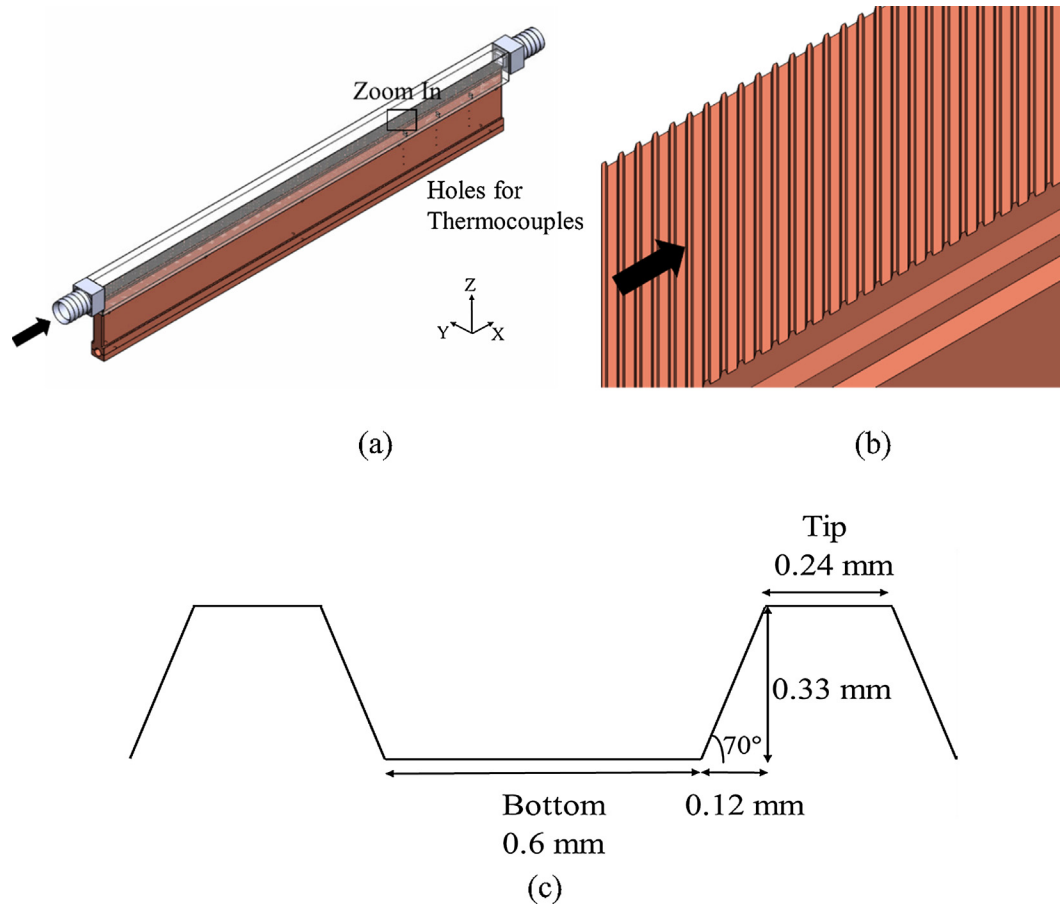
Fig. 1. (a) Schematic for test section; (b) zoom-in view at micro-fins; and (c) schematic for micro-fins.

The focus of this work was to experimentally and numerically investigate flow patterns responsible for heat transfer enhancement and understand the mechanisms behind the phenomena. Three "cases" were investigated in this study representing three different velocities: (case 1) average velocity ≈ 0.5 m/s, Reynolds number ≈ 7600; (case 2) average velocity ≈ 0.9 m/s, Reynolds number ≈ 14,000; and (case 3) average velocity ≈ 1.8 m/s, Reynolds number ≈ 28,000.

2. Experimental setup

2.1. Test section

The primary test section was a square channel with clear upper and side walls as shown schematically in Fig. 1(a). The cross-section of the channel was 15.2 mm square and 609.6 mm long. The test section had an extended length to allow study of the fully developed hydrodynamic region. Water flowed in the direction of the arrow, which was in the direction of the X-axis. There were three columns of thermocouple holes at the downstream of the copper block. PIV collected experimental results at the fully developed region in zoom-in rectangular, and its distance from the entrance was approximately 460 mm. Fig. 1(b) is a zoom-in view at the micro-fins. The micro-fins had a 45Â° helix angle. Fig. 1(c) illustrates the schematic for the micro-fins with dimensions. Height of the micro-fins was 0.33 mm. The ratio of the micro-finned area to the plain area on the bottom was 1.6. Details of the water loop system can be found in Li et al. [11].

2.2. Measurement of heat transfer coefficient

The convective heat transfer coefficient (*HTC*) was measured as a semi-local surface average [27,28]. The heat transfer coefficient was calculated as follows:

$$HTC = \frac{q''}{\Delta T} \tag{1}$$

ΔT was the difference between surface temperature and water flow temperature. The heat flux, q'' was determined from the following equation:

$$q'' = -\kappa \frac{dT(z)}{dz} \tag{2}$$

κ was thermal conductivity. Linear regression, as follows, was used to predict heat flux and surface temperature:

$$a = \bar{z} - b\bar{T} \tag{3}$$

$$b = \frac{\sum_{i=1}^{6}(T_i - \bar{T})(z_i - \bar{z})}{\sum_{i=1}^{6}(T_i - \bar{T})^2} \tag{4}$$

a was the z-intercept and b was the slope of the linear regression. b was equal to $\frac{dT(z)}{dz}$ in Eq. (2). In Fig. 1(a), there are three columns of thermocouple holes. There are six thermocouples in each column. The distance between the first top hole and the surface is 2.3 mm. The interval between each hole is 10 mm. a and b are determined by the temperature distribution in the solid copper block.
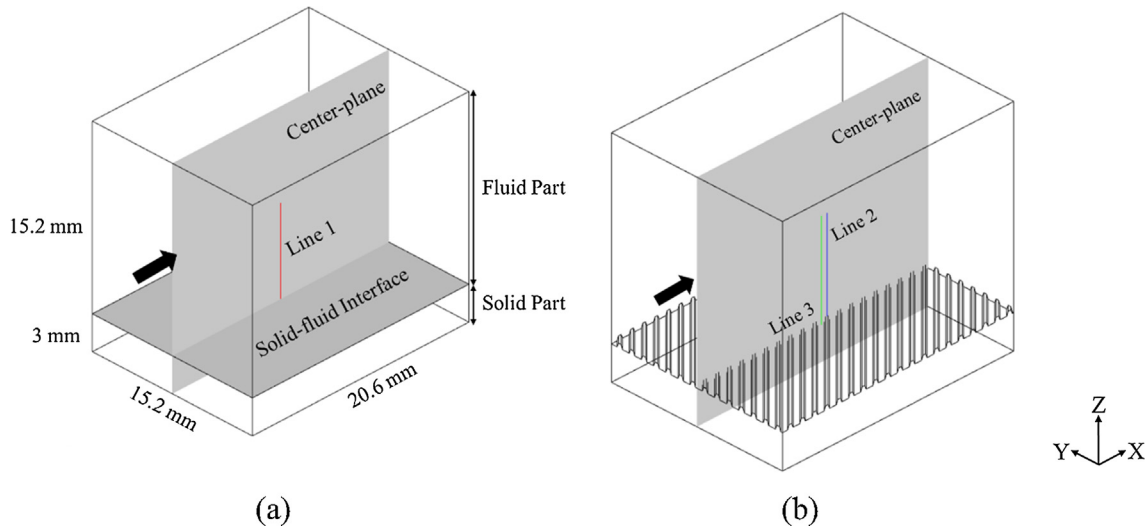
Fig. 2. Geometries (a) smooth duct and (b) micro-finned duct.

Table 1
Mesh sizes and time-step sizes.

Smooth Duct			
Velocity (m/s)	0.5	0.9	1.8
Mesh Sizes (mm)	0.30	0.25	0.20
Time Step Sizes (s)	0.0005	0.0002	0.0001
Δx^{+}, Δy^{+}	11.5	13.1	19.3
Micro-finned Duct			
Velocity (m/s)	0.5	0.9	1.8
Mesh Sizes (mm)	0.20	0.15	0.10
Time Step Sizes (s)	0.0002	0.0001	0.00005
Δx^{+}, Δy^{+}	15.9	18.5	16.3

2.3. Measurement of pressure drops

A pressure transducer from Omega Engineering Inc. was mounted in the system. Its range was from 0 to 2490.9 Pa, and

accuracy was ±0.05%. The pressure transducer was an industrial transmitter with high accuracy and low noise, 4–20 mA output. A broad temperature range and excellent temperature compensation made the pressure transducer stable at fluctuating temperatures.

2.4. Particle image velocimetry measurement and instrumentation

A commercially available, two-dimensional PIV (2D-PIV) system collected the flow characteristics. Fluorescent particles, 3.2 μm in diameter, were used for PIV measurements. Pixel size of the camera used in this experiment was 7.4 pixel/μm. Dimensions of the camera's view were 2048 pixel × 2048 pixel (3 mm × 3 mm). The view of the camera was in the X–Y plane. The camera was moved in the Z direction and was installed on a translating stage with a one-inch micrometer traverse. Movement of the camera was corrected to reflect true movement of the focal plane due to the difference in optical path length caused by the air/
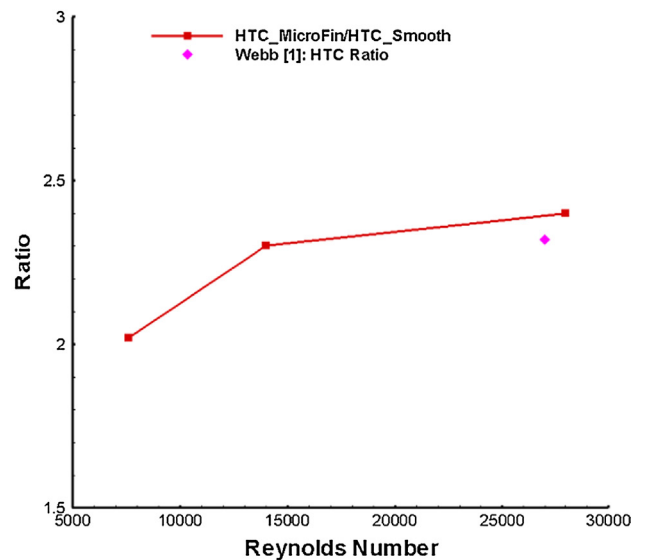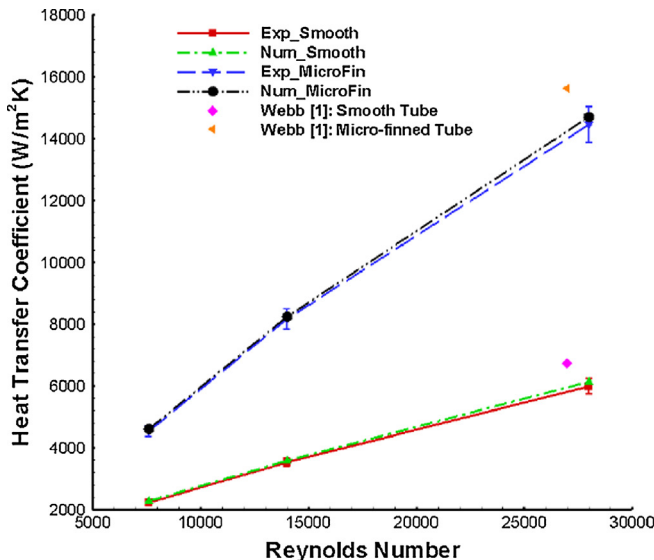

Fig. 3. (a) Experimental and numerical HTC; and (b) ratio of HTC in the micro-finned duct to HTC in smooth duct.

water interface. Therefore, the true movement was equal to the micrometer movement multiplied by the refractive index of water, 1.33 [29,30].

INSIGHT 4G was used for global image capture, analysis, and display purposes [31]. It implemented the PIV processing algorithm in the following four plugin engines: (1) grid engines, (2) spot mask engines, (3) correlation engines, and (4) peak engines. Nyquist grid, Gaussian mask, fast Fourier transform correlation, and Gaussian peak, respectively, were applied to data processing. Details of the PIV measurement can be found in Li et al. [11].

3. Flow characteristics from PIV data

PIV data measures velocity magnitude and turbulent kinetic energy. The velocity magnitude combines the velocity components in three directions as follows:

$$U = \sqrt{(u_x^2 + u_y^2 + u_z^2)} \tag{5}$$

The turbulent kinetic energy (TKE) is the kinetic energy per unit mass of the turbulent fluctuations u_i' in a turbulent flow. The unit of TKE is m^2/s^2. The equation of TKE is

$$TKE = \frac{1}{2}(\overline{u_x'^2} + \overline{u_y'^2} + \overline{u_z'^2}) \tag{6}$$

where the overbar indicates a time average. For the work in this paper, these averages were calculated from a series of 2000 PIV images. For 2D-PIV, the third velocity component u_z was not measured, so we assumed velocity components and turbulent fluctuations in the Z direction were the same as those in Y direction.
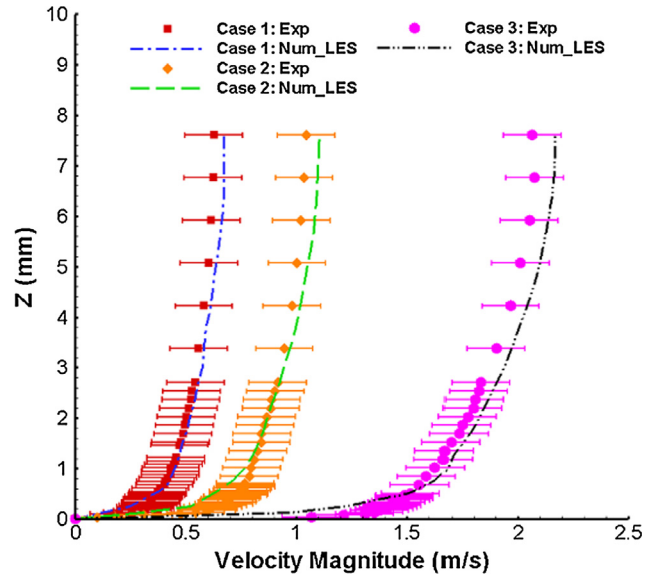

Fig. 5. Experimental and numerical velocity profiles on line 1 in the smooth duct.

4. Measurement uncertainties

Uncertainty analyses were performed for HTC and PIV measurements to judge the accuracy of the experimental results. Based on the calculation of HTC in Section 2.2, the uncertainty of the HTC was determined by
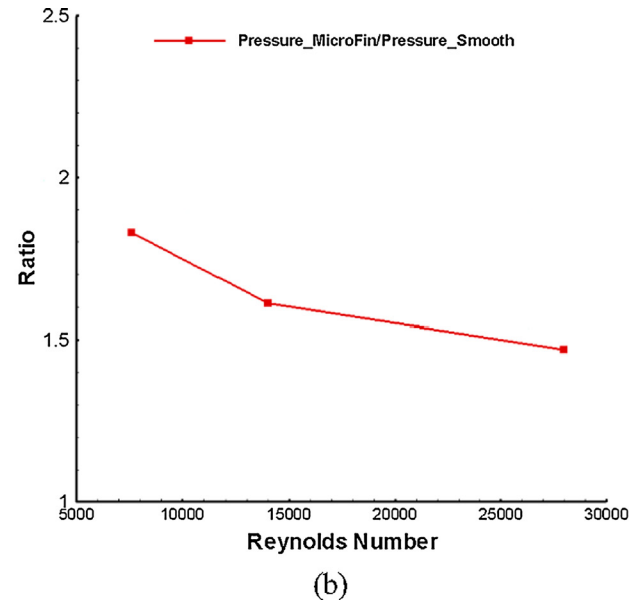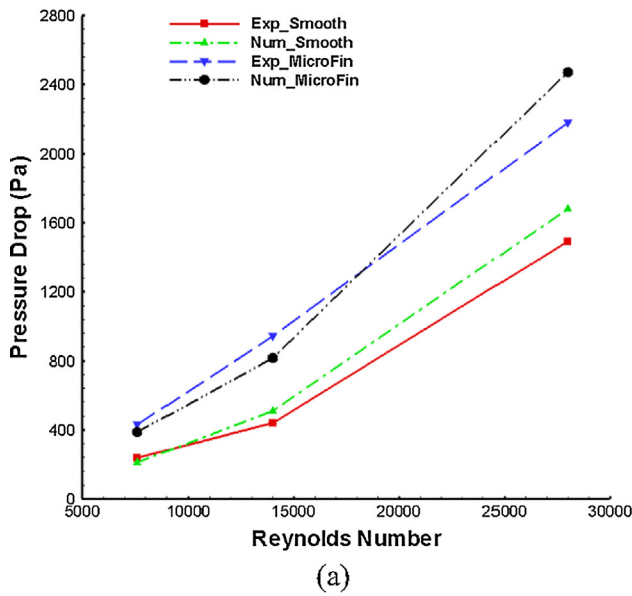

Fig. 4. (a) Experimental and numerical pressure drop; and (b) ratio of pressure drop in the micro-finned duct to that in smooth duct.

Table 2
HTC and pressure drops for case 2 with different turbulent models.

	Experimental	LDKM	Lilly	WMLES	RSM	Realizable k-ε
HTC (W/(m²·K))	8153.6	8249.4	9792.3	9945.6	8873.1	6112.8
Relative Error of HTC	N/A	1.2%	20.1%	22.0%	8.8%	25.0%
Pressure (Pa)	941.4	817.2	733.7	752.7	791.6	648.6
Relative Error of Pressure	N/A	13.2%	22.0%	20.0%	15.9%	31.1%

$$UN_{HTC} = \left[\left(\frac{\partial HTC}{\partial un_{q''}} \cdot un_{q''}\right)^2 + \left(\frac{\partial HTC}{\partial un_{T_{surf}}} \cdot un_{T_{surf}}\right)^2 + \left(\frac{\partial HTC}{\partial un_{T_{flow}}} \cdot un_{T_{flow}}\right)^2\right]^{1/2}$$

(7)

where the un is an uncertainty of each source. Due to the heat flux and surface temperature were calculated by linear regression. Eq. (7) is converted to the following format:

$$UN_{HTC} = \left[\left(\frac{\partial HTC}{\partial un_a} \cdot un_a\right)^2 + \left(\frac{\partial HTC}{\partial un_b} \cdot un_b\right)^2 + \left(\frac{\partial HTC}{\partial un_z} \cdot un_z\right)^2 \right.$$
$$\left. + \left(\frac{\partial HTC}{\partial un_{T_{flow}}} \cdot un_{T_{flow}}\right)^2\right]^{1/2}$$

(8)

Maximum HTC uncertainty was $\pm 4\%$. The main uncertainty for the HTC measurement was from the slope of the linear regression, b. The linear slope increased as the power of the heater increased, which led to the decrease of slope uncertainty. Uncertainty for HTC was low because a high-power heater was used in the study. An uncertainty analysis of the PIV data was presented in Li et al. [11,32] and revealed an uncertainty of ± 0.13 m/s.

5. Numerical simulations

The numerical simulations, once validated, provided deeper insight into the flow structures occurring around the fins. The general simulation used mass flow rates in case 1, case 2 and case 3 as 0.12 kg/s, 0.22 kg/s and 0.44 kg/s, respectively. Upstream bulk
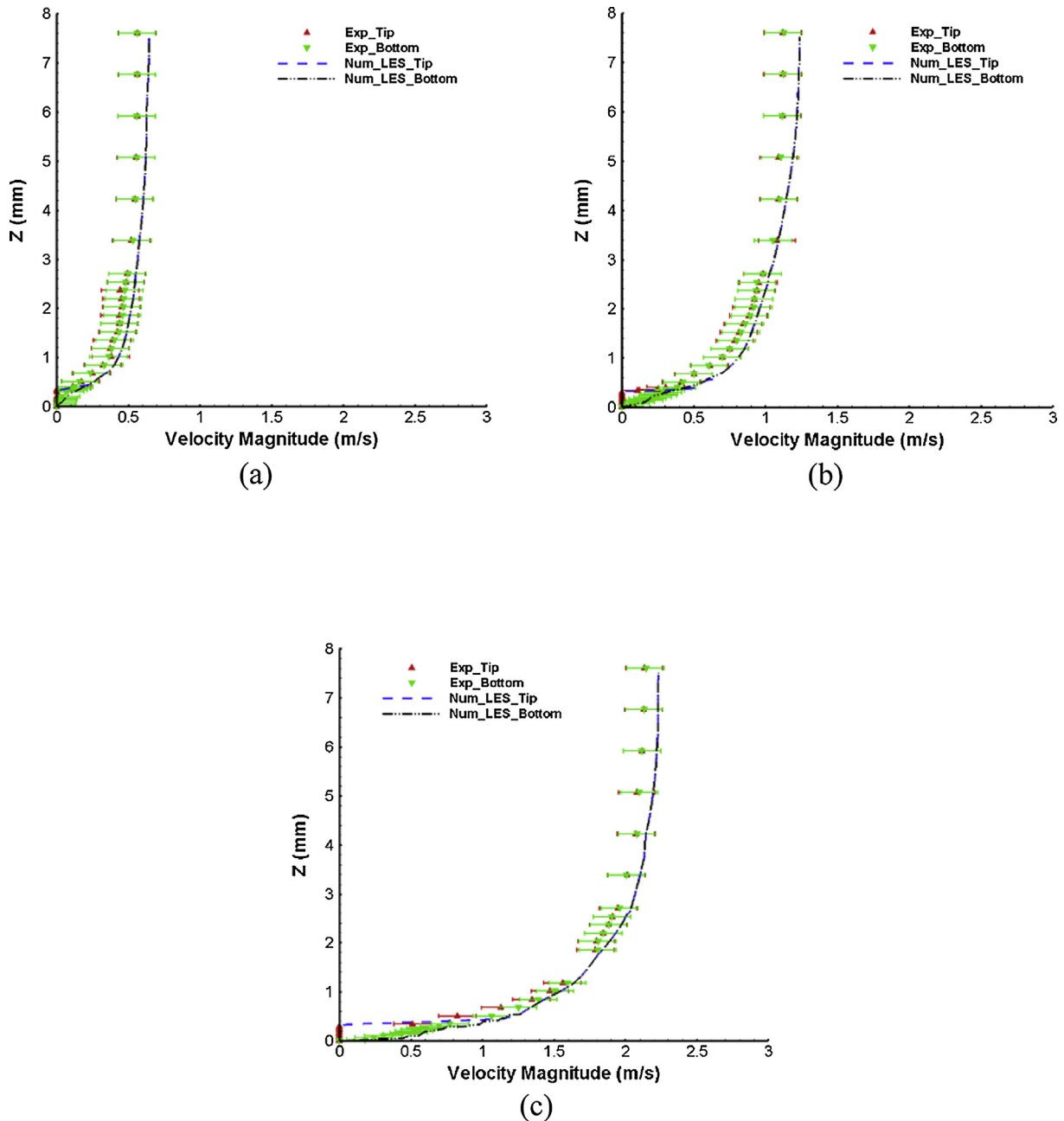

Fig. 6. Experimental and numerical velocity profiles on lines 2 and 3 in the micro-finned duct (a) case 1, (b) case 2, and (c) case 3.

temperatures were 300 K. Temperatures on the bottoms of the solid part were 305 K. The solid-fluid interface was specified as a coupled wall. Both conductive and convective heat transfer were simulated in the study. Numerical data were collected and processed after a three-second running time to make sure the flow had fully developed. Other details on the numerical setup are given below.

5.1. Flow models

In this study, Navier-Stokes equations were used to simulate the fluid transport process. The equation for conservation of mass, or continuity equation, is written as follows [24,33]:

$$\frac{\partial \rho}{\partial t} + \nabla \cdot \left(\rho \vec{u} \right) = 0 \tag{9}$$

In this equation, ρ is fluid density and u is fluid velocity.

Conservation of momentum in an inertial reference frame is described by [24,34]

$$\frac{\partial}{\partial t} \left(\rho \vec{u} \right) + \nabla \cdot \left(\rho \vec{u} \otimes \vec{u} \right) = -\nabla p + \nabla \cdot \left(\overline{\overline{\tau}} \right) + \rho \vec{g} + \vec{F} \tag{10}$$

where p is the static pressure; $\overline{\overline{\tau}}$ is the stress tensor; and $\rho \vec{g}$ and $\vec{F}$ are the gravitational body force and external body forces, respectively.

5.2. Viscous models

To simulate the process of fluid mixing caused by flow separation and reattachment, LES with LDKM was applied to the numerical simulations. LES is a popular technique for simulating turbulent flows, which allows one to solve for the large eddies in a calculation explicitly and account for the small eddies by using a sub-grid scale model implicitly. Mathematically, one may think of separating the velocity field into resolved and sub-grid parts. Formally, one may think of filtering as the convolution of a function with [33]

$$\overline{u}_i \left(\vec{x} \right) = \int G(\vec{x} - \vec{\xi}) u(\vec{\xi}) d\vec{\xi} \tag{11}$$

resulting in

$$u_i = \overline{u}_i + u_i' \tag{12}$$

where $\overline{u}_i$ is the resolvable scale part and u_i' is the sub-grid scale part. The research was focused on LES of incompressible flows. The decomposition parts, $u_i = \overline{u}_i + u_i'$ and $p = \overline{p} + p'$, were substituted into incompressible Navier-Stokes equations:

$$\frac{\partial \overline{u}_i}{\partial x_i} = 0 \tag{13}$$

$$\frac{\partial \overline{u}_i}{\partial t} + \overline{u}_j \frac{\partial \overline{u}_i}{\partial x_j} = -\frac{\partial}{\partial x_j} \left(\overline{p} \delta_{ij} + \tau_{SGS_{ij}} \right) + v \frac{\partial^2 \overline{u}_i}{\partial x_j \partial x_j} \tag{14}$$

δ is Delta function. v is the kinematic viscosity. The subgrid-scale stress, $\tau_{SGS_{ij}}$, is modeled by

$$\tau_{SGS_{ij}} = \overline{u_i u_j} - \overline{u}_i \overline{u}_j \tag{15}$$

The subgrid-scale kinetic energy for LDKM is defined as [25]

$$k_{SGS} = \frac{1}{2} (\overline{u_k^2} - \overline{u}_k^2) \tag{16}$$

The subgrid-scale stress can then be written as

$$\tau_{SGS_{ij}} = -2C_k k_{SGS}^{1/2} \overline{\Delta} \overline{S}_{ij} + \frac{2}{3} k_{SGS} \delta_{ij} \tag{17}$$

where $\overline{\Delta}$ is grid width. $\overline{S}_{ij}$ is the resolved-scale strain-rate tensor, which is defined as

$$\overline{S}_{ij} = \frac{1}{2} (\frac{\partial \overline{u}_i}{\partial x_j} + \frac{\partial \overline{u}_j}{\partial x_i}) \tag{18}$$

This derived the transport equation for LDKM as [25]

$$\frac{\partial k_{SGS}}{\partial t} + \overline{u}_i \frac{\partial k_{SGS}}{\partial x_i} = -\tau_{SGS_{ij}} \frac{\partial \overline{u}_i}{\partial x_j} - C_\varepsilon \frac{k_{SGS}^{3/2}}{\overline{\Delta}} + \frac{\partial}{\partial x_i} \left(\mu_t \frac{\partial k_{SGS}}{\partial x_i} \right) \tag{19}$$

In the above equations, model constants, C_k and C_ε, were determined dynamically. For LDKM, the subgrid-scale eddy viscosity, μ_t, was modeled by [24,25]

$$\mu_t = C_k \overline{\Delta} k_{SGS}^{1/2} \tag{20}$$

Some other viscous models, such as the Smagorinsky-Lilly Model (Lilly model), Algebraic Wall-Modeled LES Model (WMLES model), and Reynolds Stress Equation Model (RSM), etc., were also tried in the study. It was found these viscous models failed to validate against the experimental data.

5.3. Energy equations

The energy equation for LES is solved in the following form [23,24]:

$$\frac{\partial \overline{T}}{\partial t} + \nabla \cdot \left(\overline{u} \overline{T} \right) = \nabla \cdot \left(\beta \nabla \overline{T} \right) - \frac{\nabla \cdot q_{SGS}''}{\rho e} \tag{21}$$

$\overline{T}$ is filtered temperature for LES. β and e are thermal diffusivity and heat capacity, respectively. q_{SGS}'' is subgrid-scale heat flux.

5.4. Geometries and mesh sizes

The simulation was conducted in a short duct with periodic boundary conditions, as shown in Fig. 2, to reduce computational time. The upper part was a square duct with water flow. Height and the width of the fluid part were 15.2 mm. Total length of the numerical geometry was 20.6 mm. In the duct with smooth surfaces, Line 1 in Fig. 2(a) was the location where experimental results and numerical results were compared. Line 1, starting from the solid–fluid interface, was at the center of the interface. Lines 2 and 3 in Fig. 2(b) showed the positions where results were output
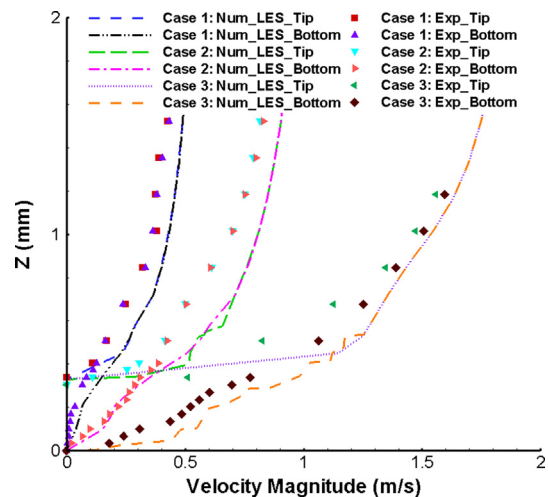
Fig. 7. Zoom-in view of experimental and numerical velocity profiles in the micro-finned duct for the three cases.

for the micro-finned duct. Line 2 was from the tip of the micro-fins and Line 3 was from the bottom of the micro-fins. Center planes are shown in Fig. 2(a) and (b). Arrows in Fig. 2 illustrate the direction of water flow.

Mesh sizes for LES are dependent on the Reynolds numbers. If mesh sizes are too coarse, it can lead to a bad prediction of flow characteristics. Typical resolution requirements for LES are [24]

$$\Delta x^+ = 40 \tag{22}$$

$$\Delta y^+ = 20 \tag{23}$$

where Δx^+ is the non-dimensional grid spacing in the streamwise direction and Δy^+ in the span-wise, with the definitions as follow:

$$\Delta x^+ = \frac{u_\tau \Delta x}{v} \tag{24}$$

$$\Delta y^+ = \frac{u_\tau \Delta y}{v} \tag{25}$$

In the study, Δx was equal to Δy. Therefore, Δx^+ was equal to Δy^+. Wall friction velocity, u_τ, was defined as

$$u_\tau = \sqrt{\frac{\tau_w}{\rho}} \tag{26}$$

where τ_w was wall shear stress. Wall shear stresses are calculated by pressure drops in the experiments. Mesh sizes for all cases are shown in Table 1. The mesh around the solid-fluid interfaces required special attention to improve the numerical prediction of HTC. Face sizing was applied to both sides (i.e., solid side and fluid side) of the interface to make the mesh changing around the interface go smoothly. Time-step sizes shown in Table 1 satisfy the equation, $dt \leq \frac{\Delta}{U}$ [35].
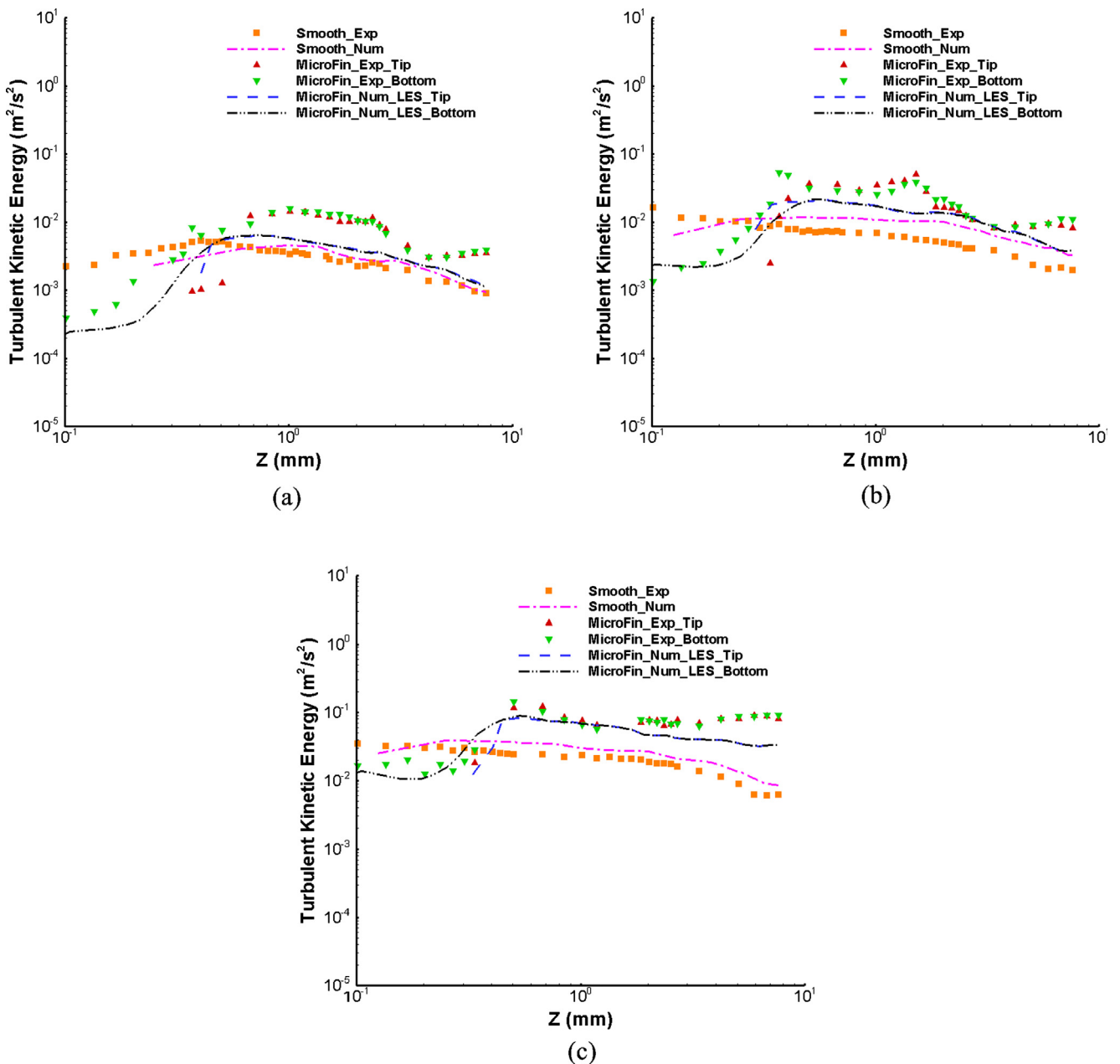

Fig. 8. Experimental and numerical *TKE* profiles on lines 1, 2, and 3 in the smooth and micro-finned duct (a) case 1, (b) case 2, and (c) case 3.

6. Validation and comparison

For validation and further discussion, *HTC*, pressure drops, velocity profiles, *TKE* profiles, and vector fields in the numerical simulations were compared with those in the experiment.

6.1. Heat transfer coefficient and pressure drops

Fig. 3(a) shows the experimental and numerical heat transfer coefficient for all cases with uncertainty. The experimental results matched the numerical results very well. All numerical results were within the uncertainty. The heat transfer coefficient increased with the increase of the Reynolds number. The heat transfer coefficients in the micro-finned duct were higher than those in the smooth duct. Fig. 3(b) demonstrates the ratio of heat transfer coefficient in the micro-finned duct to that in the smooth duct. The ratio in transition flow was relatively lower than those in the fully developed flow. Furthermore, the ratio of heat transfer coefficient was higher than that of area increase (1.6 times). There-fore, enhanced areas of the surfaces were not the only reason for the increase in heat transfer coefficient. Fig. 3(a) and (b) also show Webb's results [1]. Although the micro-fins in Webb's paper were in a circular pipe, results measured in the study were still close to theirs.

Experimental and numerical pressure drops are shown in Fig. 4 (a). The maximum relative error between the experimental results and numerical results was approximately equal to 15 percent. Peri-odic boundary conditions used in the numerical simulations mainly caused the relative error. Fig. 4(b) shows the ratio of pres-sure drop in the micro-finned duct to that in the smooth duct. The ratio decreased with the increase of Reynolds number. Based on Figs. 3(b) and 4(b), the micro-fins were better suited for the high Reynolds number cases (around $Re \approx 28,000$).

Table 2 shows the *HTC* and pressure drops for case 2 with differ-ent turbulent models. The numerical results were compared with the experimental results. After the comparison, the numerical sim-ulation with LDKM had the smallest relative error for the predic-tion of *HTC* and pressure drop. Therefore, LES with LDKM was selected to use in the study.

6.2. Velocity profiles

Fig. 5 displays velocity profiles on line 1 in the smooth duct for the three cases. Y-axis, i.e., Z (mm), represents the distance from the location of the velocity magnitude to the bottom of the duct. It is obvious the velocity profiles simulated by LES with LDKM matched the PIV results very well.

The numerical velocity profiles in the micro-finned duct simu-lated by LES on lines 2 and 3 are shown in Fig. 6(a)–(c). The Y-axis in Fig. 6 represents the distance from the velocity location to the bottom of the micro-fins. Therefore, the velocity profiles within the region, $Z \leq 0.33$ mm (micro-fin height), were all zeros. Numer-ical velocity profiles agreed with those measured by PIV very well. Numerical velocity profiles were all within the uncertainty of the experimental velocity profiles. Fig. 7 illustrates the zoom-in view of experimental and numerical velocity profiles near the bottom region in the micro-finned duct for the three cases. The increasing slopes of the velocity profiles above the micro-fin bottom were dif-ferent from those on the tip. The difference can be seen in the region around $Z = 0.33$ mm. Then the velocity profiles from the tip and the bottom of the micro-fin merged with the increase of Z. Therefore, the micro-fins affected the surrounding velocity pro-files significantly.

6.3. Turbulent kinetic energy profiles

Fig. 8(a)–(c) show the experimental and numerical *TKE* profiles on lines 1, 2, and 3 for the three cases, respectively. The experimen-tal *TKE* profiles agreed with the numerical results very well. The *TKE* profiles for the micro-finned duct within the region, $Z \leq 0.33$ mm, were lower than those for the smooth duct. *TKE* was weak-ened within the region by the gap between two micro-fins. Then *TKE* in the micro-finned duct increased, with Z increasing until $Z \approx 0.5$ mm. Different regions of the micro-fins disturbed the *TKE* differently.

6.4. Vector fields

Fig. 9(a) and (b) show the transient vector fields' output from the PIV data and numerical simulations, respectively, in the X-Y
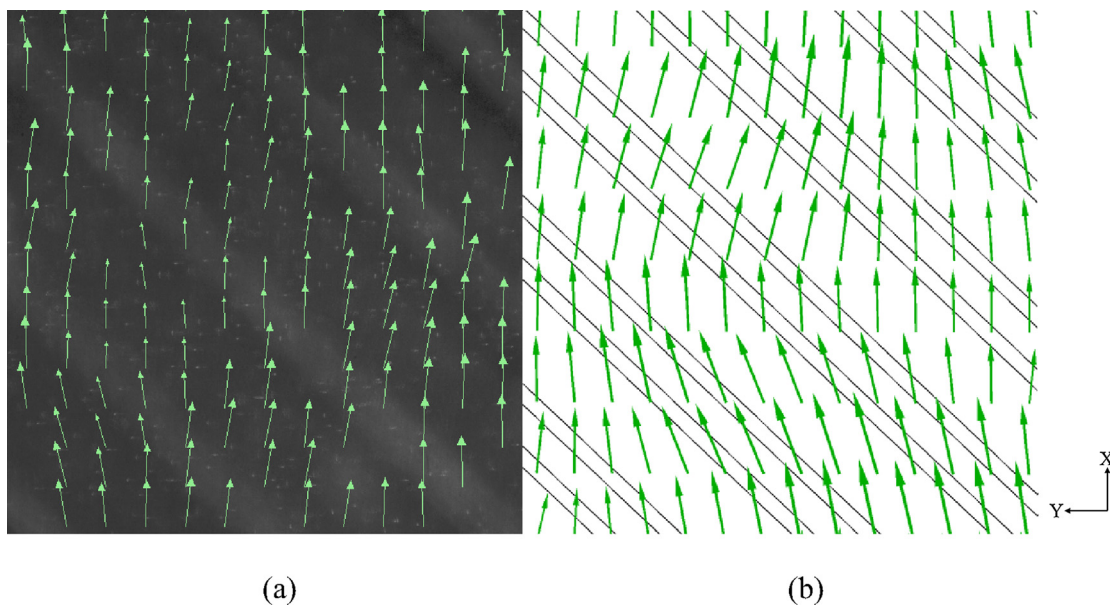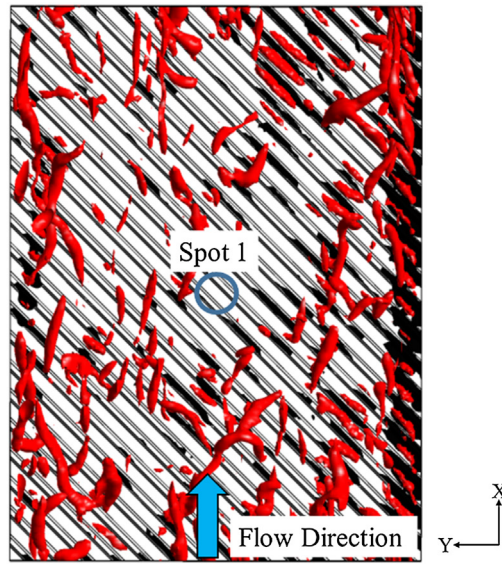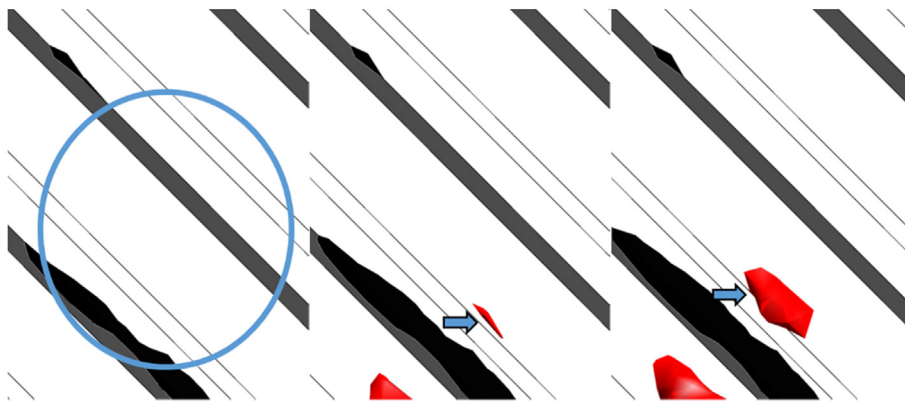

Fig. 9. Transient vector fields' output from (a) PIV data and (b) numerical simulations.

Fig. 10. (a) Q criterions ($Q = 50,000$ s^{-2}) and heat flux for case 1 at 5.5 s; (b–h) are zoom-in views of spot 1 at (b) 5.503 s, (c) 5.504 s, (d) 5.505 s, (e) 5.506 s, (f) 5.507 s, (g) 5.508 s, and (h) 5.509 s.

plane of the micro-finned duct for case 2. The size of the two domains was 3 mm × 3 mm, which was the same as the PIV camera's view. Location of the plane was 1 mm above the tips of the micro-fins. The micro-fins were still seen in the PIV image. In general, vector fields in the numerical simulation were similar to those in the experiment. Similar flow patterns existed around the region.

7. Results and discussion

Relationships between the flow pattern and heat transfer are highlighted in this section. Wall-bounded turbulent flows can generally be broken into three zones: viscous region, log-law region, and bulk flow zones. Two of these zones are particularly important to the micro-fin. Zone 1 (viscous region) here is defined as the gaps between the micro-fins. Zone 2 (log-law region) is the location above the tips of the micro-fins, and here is defined as a height of 4 mm above the fin.

7.1. Relationships between Q criterions and heat flux

Fig. 10(a) shows the Q criterion in zones 1 and 2 for case 1 in the 3D domain at 5.5 s. The Q criterion value in Fig. 10(a) is 50,000 s^{-2}. Black colors on the interface are locations where the heat flux was greater than 20,000 W · m^{-2}, which is approximately equal to the double average heat flux for case 1. In Fig. 10(a) with Q = 50,000 s^{-2}, the coherent structures generally corresponded to the heat flux. To further analyze details of relationships between the coherent structures and the heat flux, spot 1 in Fig. 10(a) was zoomed-in on and shown in Fig. 10(b)–(h). At t = 5.503 s, there were no coherent structures with Q = 50,000 s^{-2} in the spot. Then after a short time, at t = 5.504 s, a tiny coherent structure was generated (an arrow points out the coherent structure). After 0.001 s more, the coherent structure became larger in Fig. 10(d). With growth of the coherent structure, a location with the heat flux greater than 20,000 W · m^{-2} (an arrow points it out) gradually appeared in Fig. 10(e). This high-heat flux region appeared on the next downstream micro-fin face, because the coherent structure
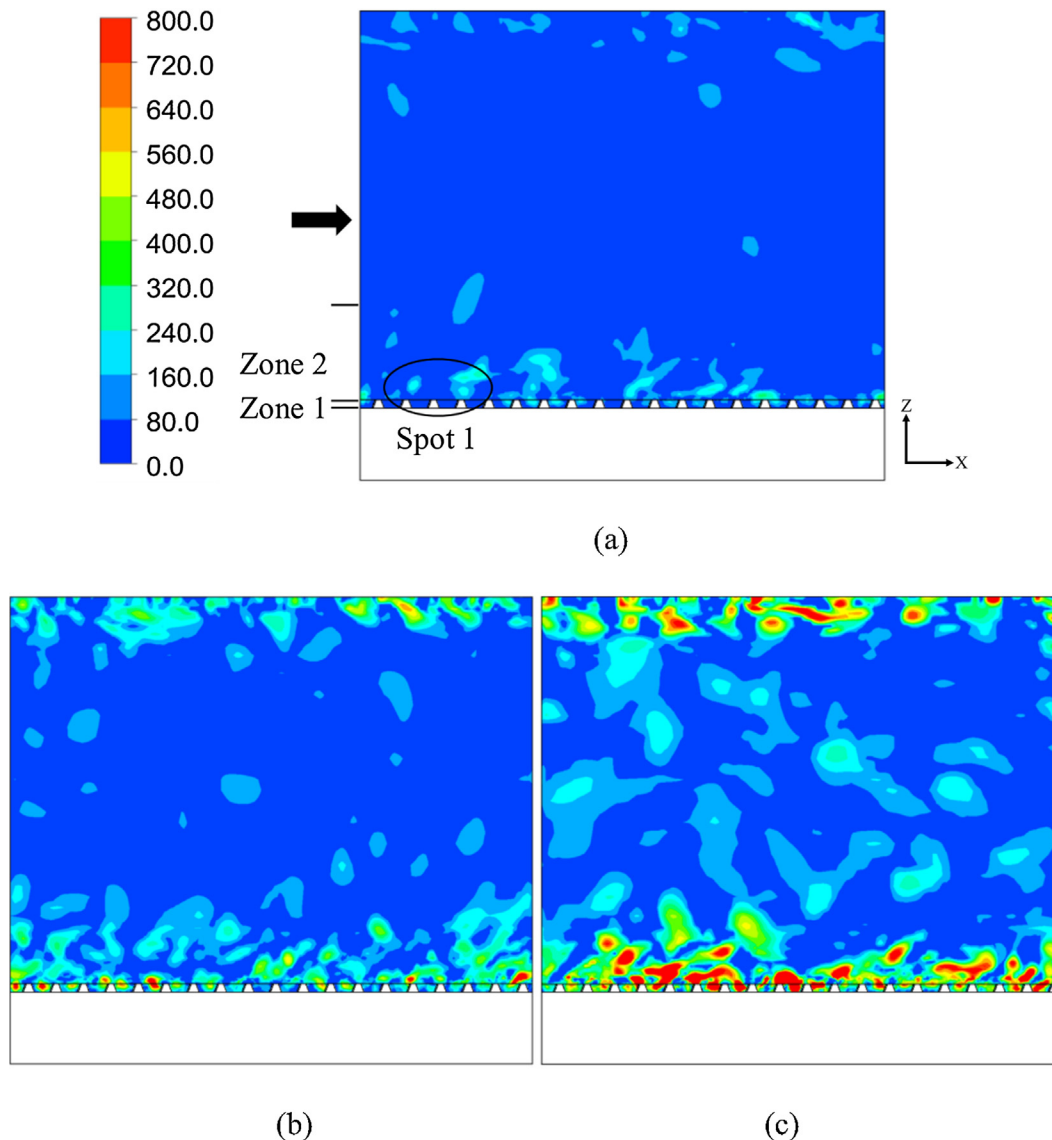

(a)

(b)   (c)

Fig. 11. Contours of velocity swirling vector at 5.501 s (a) case 1, (b) case 2, and (c) case 3.

showed the development of a swirl caused by flow separation. According to Fig. 10(f)–(h), size of the area for the heat flux increased with growth of the coherent structure, which directly demonstrated that the coherent structure affected high-heat flux greater than 20,000 W · m^{-2}.

7.2. Swirls in zone 1 and zone 2

Fig. 11 shows the contours of velocity-swirling vectors for the three cases at $t = 5.501$ s on the center plane. The arrow shows the direction of water flow. The figure clearly highlights the difference in transition and fully turbulent flows. Fig. 11(b) and (c) show nearly every fin gap has significant swirl while the lowest Reynolds number has very few. Spot 1 in Fig. 11(a) shows significant swirls existing above the fin. The larger swirls pass by the micro-fins in zone 2, but are not strong enough to penetrate zone 1 completely. The swirls in zone 1 reinforce the fluid mixing between zones 1 and 2, which enhances the heat transfer between the two zones. This is one reason why the higher heat-transfer-enhanced ratio occurs in the turbulent flow region (one answer for the second

problem in the introduction). It should be noted that Fig. 11 represents one moment in time and is not an average plot.

The LES simulations can also be used to study the dynamic formation and decay of the swirls between the fins hinted at in the previous figures. Fig. 12 shows a time-resolved set of plots for case 2. The swirl structures shown in zones 1 and 2 can be seen moving and evolving. Extended movies show the swirl structures between the fins forming when larger structures in zone 2 pass over the fin. In some cases, intense swirls can be seen jumping to the next fin passage. Fig. 10 highlights the formation of these more-intense inter-fin swirls are associated with high-heat fluxes and thus enhanced heat transfer. Another observation was that fluid mixing between zone 2 and the bulk flow occurs much more often for cases 2 and 3.

7.3. Temperature contours on the center plane

Fig. 13 illustrates temperature contours for the three cases in the smooth duct. There are clear temperature sublayers from the bottom to the top in the domain. It is easy to distinguish temperature contours layer by layer, even for case 3 with the highest
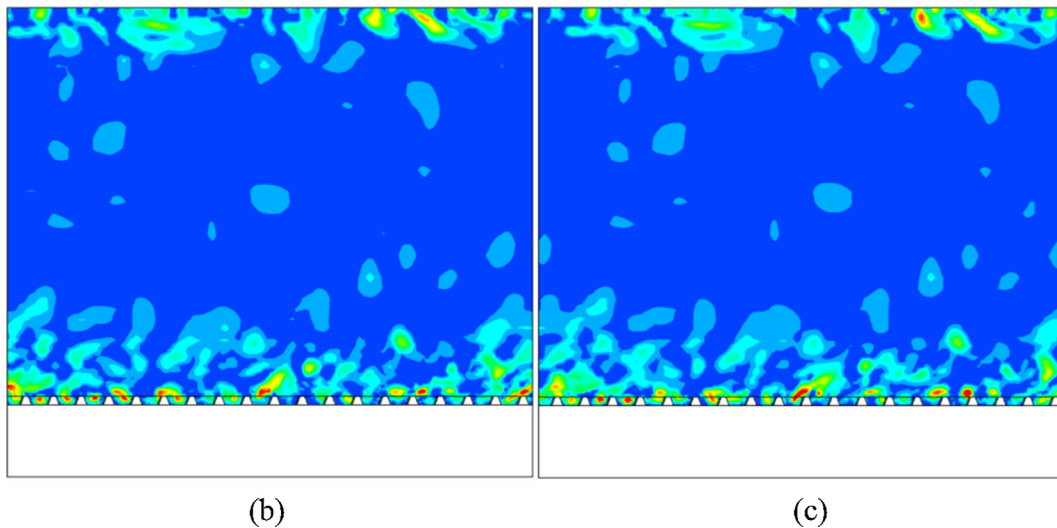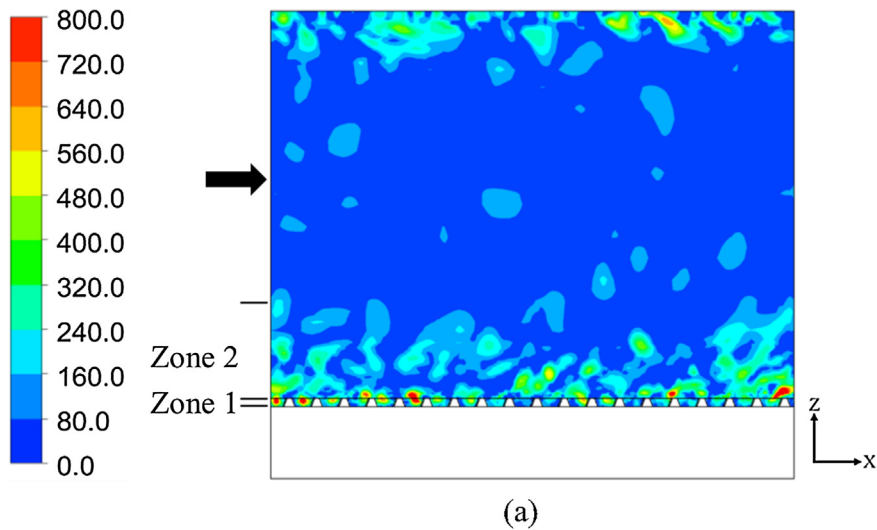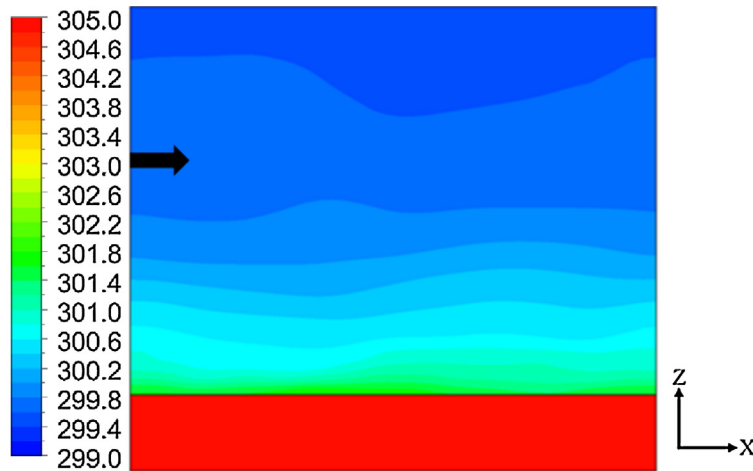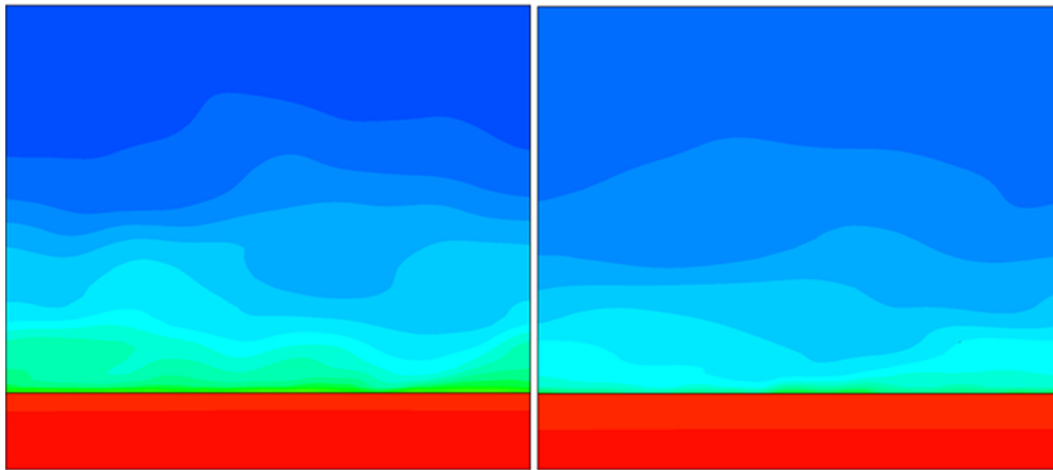

Fig. 12. Contours of velocity swirling vector for case 2 at (a) 5.501 s, (b) 5.502 s, and (c) 5.503 s.

Fig. 13. Temperature contours in the smooth duct at 5.5 s (a) case 1, (b) case 2, and (c) case 3.

Reynolds number. Fig. 14 displays temperature contours for the three cases in the micro-finned duct. In Fig. 14(a), the temperature contours became unstable and the cool water in zone 3 penetrated almost entirely through zone 2 to the micro-fin surface. This process created large oscillation of temperature boundary layers. In Fig. 14(b) and (c), the process is enhanced with the Reynolds number, and temperature contours are broken and compressed indicating higher heat transfer coefficients. Fluid mixing among the different temperature layers enhances the heat transfer coefficient in the micro-finned surface.

7.4. Velocity contours on the center plane

Fig. 15 illustrates velocity contours in the smooth duct and micro-finned duct for case 2. Fig. 15 is taken from the same time step as Figs. 13 and 14 and thus can be directly compared. First, it is interesting to compare velocity contours between smooth and micro-finned surfaces. Disruption of the zone 2 velocity profiles is clear. This disruption led to higher velocity gradients at the wall, and thus the increased pressure drop was associated with the micro-finned surfaces. The pressure drop was composed of

shear and pressure drag, and the later could not be seen on the plots, so an incomplete picture was presented. Mann et al. [36] have more information on the shear and pressure components of the pressure drop for such micro-finned surfaces. It is also useful to compare the temperature contour plots with the velocity plots. Water has a higher Prandtl number, so we did not expect identical contour plots. Some structures in zone 2 between Figs. 14 and 15 are the same. This is an area of active research and more study.

7.5. Distributions of coherent structures

Figs. 16 and 17 give another import view of the flow structures within the duct. These figures used Q criterions of 50,000 s^{-2} in the smooth duct and in the micro-finned duct, respectively, for the three cases. It is noticeable the coherent structures rose with the increase of the Reynolds number. There were no coherent structures with Q = 50,000 s^{-2} in Fig. 16(a). Comparing Figs. 16 and 17, when the Reynolds number was identical, there were more coherent structures in the micro-finned duct. The micro-fins on the bottom enhanced the production of the coherent structures, which improved the fluid mixing. The fluid mixing generated an
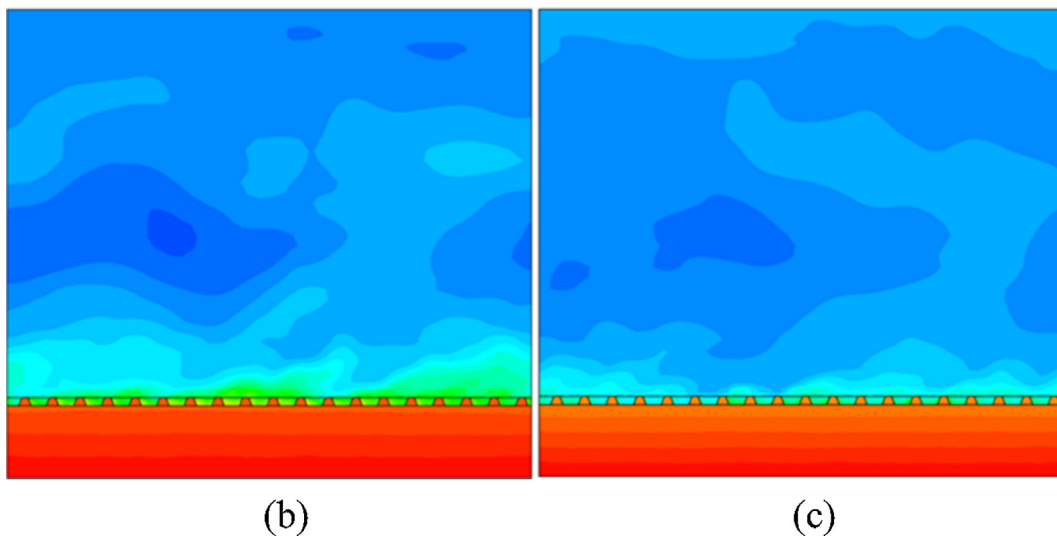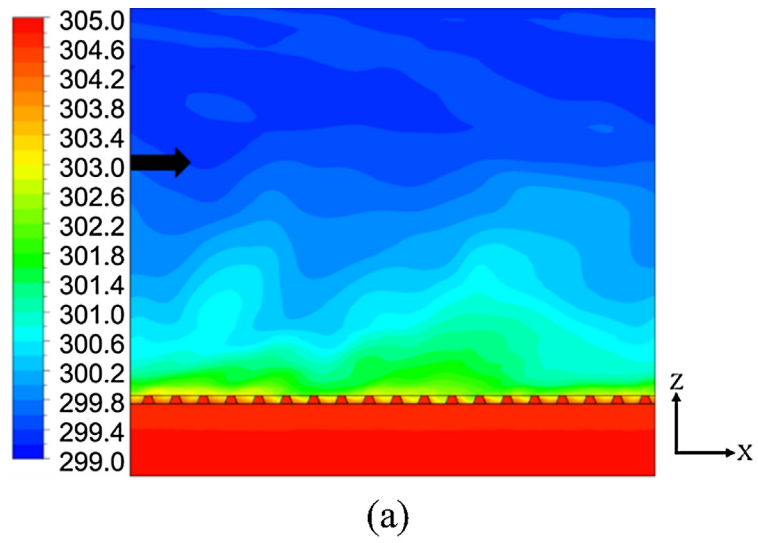
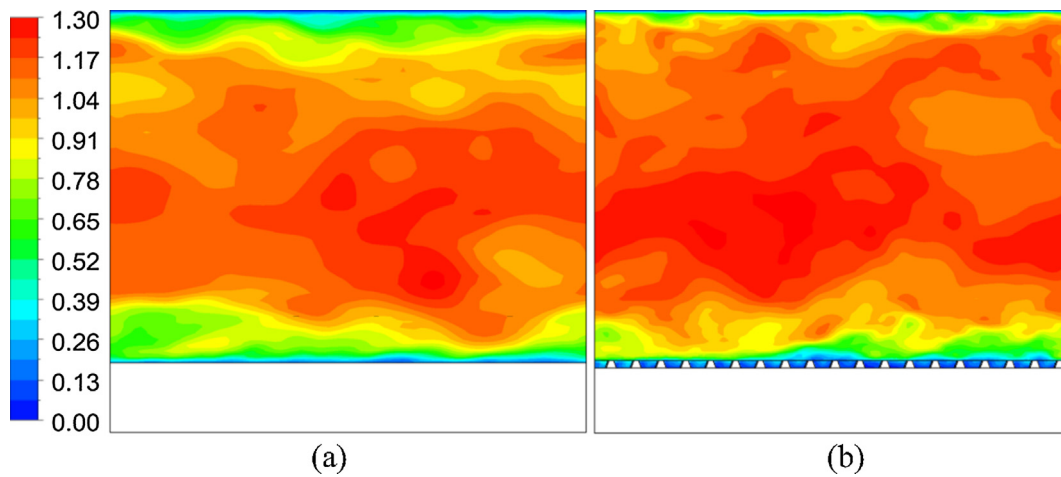Fig. 14. Temperature contours in the micro-finned duct at 5.5 s (a) case 1, (b) case 2, and (c) case 3.

Fig. 15. Velocity contours for case 2 at 5.5 s (a) smooth duct, and (b) micro-finned duct.
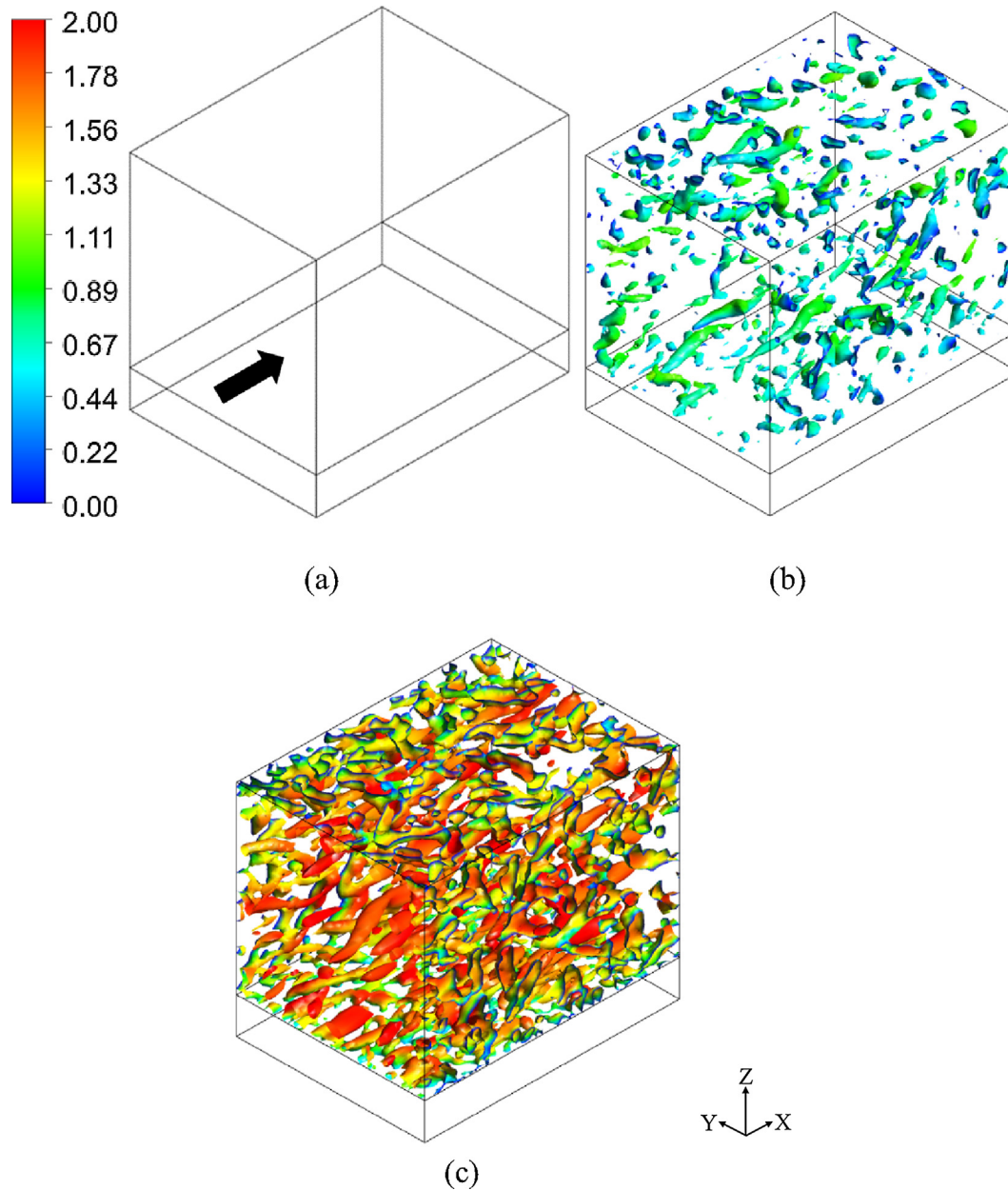
Fig. 16. Q criterions (Q = 50,000 s^{-2}) at 5.5 s in the smooth duct (a) case 1, (b) case 2, and (c) case 3.

effect to enhance the communications among the different temperature layers, which increased the heat transfer coefficient in the micro-finned duct. The micro-fins in the duct not only increased the area of the solid-fluid interfaces but also boosted the fluid mixing among the different temperature layers. Due to the bonus effect of the micro-fins, increases of heat transfer were larger than the area increases in the micro-finned tubes (one answer for the first problem in the introduction).

8. Conclusions

PIV technology and numerical simulations with LES were used to study the relationship between flow characteristics and heat transfer in a square duct with micro-fins. Good agreements were found when the experimental results were compared to the numerical simulation results. The conclusions are presented as follows:

(1) Micro-fins affected the surrounding flow characteristics significantly. Furthermore, different regions of the micro-fins disturbed the *TKE* differently.
(2) The study proved the coherent structures had some relationship to heat transfer enhancement. In the future, it would be helpful if some formulas were mathematically generated to link the coherent structures with heat transfer.
(3) Micro-fins in the duct not only enhanced the area of the solid-fluid interface but also boosted the product of coherent structures. The coherent structures contributed to the fluid mixing. The fluid mixing was an effect to enhance communication among the different temperature layers, which led to increased *HTC*. The bonus effect of the micro-fins explained the first problem of why increases of heat transfer were normally larger than area increases in the micro-finned tubes.
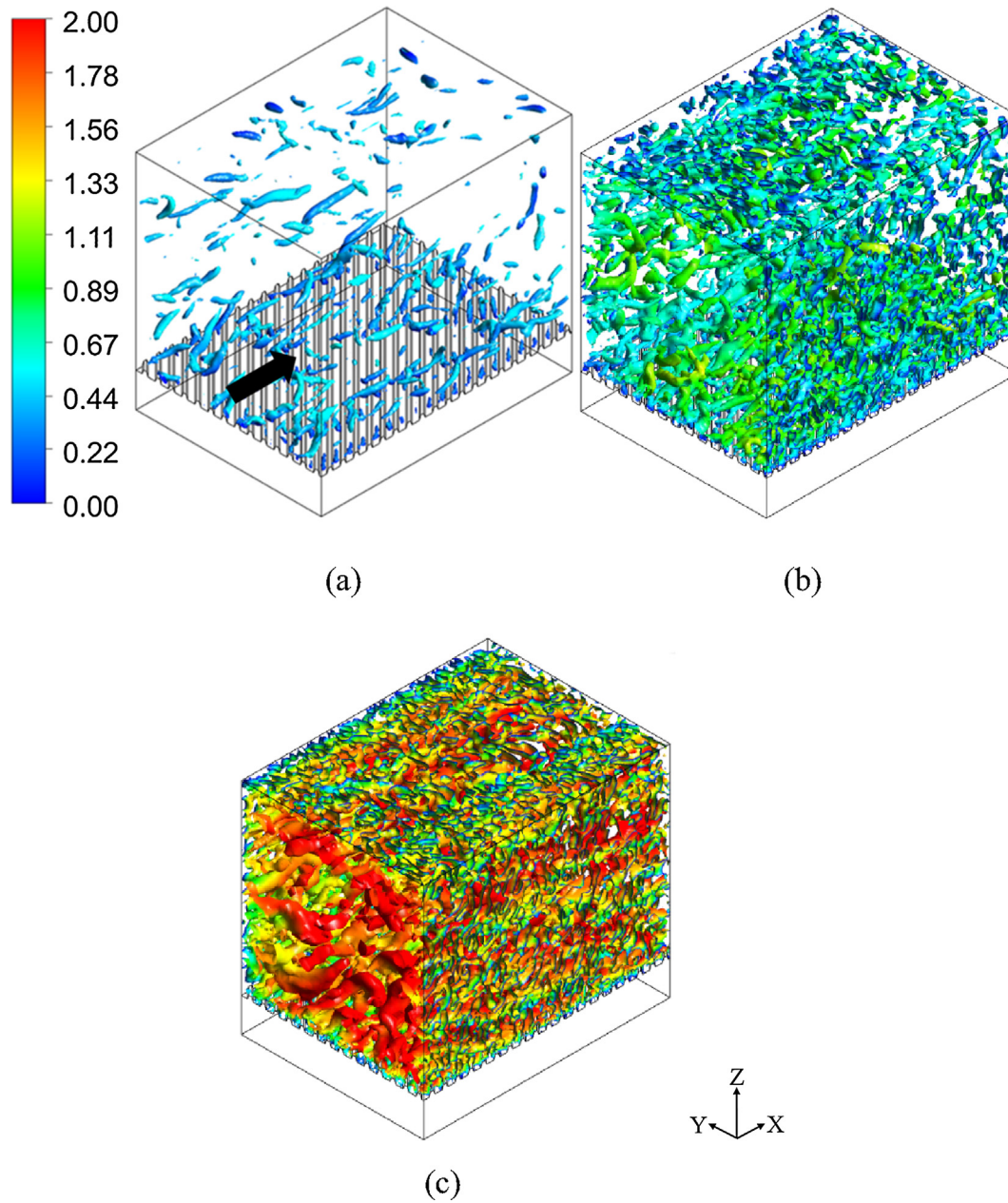
Fig. 17. Q criterions ($Q = 50,000$ s^{-2}) at 5.5 s in the micro-finned duct (a) case 1, (b) case 2, and (c) case 3.

(4) Reynolds numbers also affected the enhancement of heat transfer. Reynolds numbers predicted flow patterns in different fluid-flow situations. At a low Reynolds number, such as laminar and transition flow, some gaps of the micro-fins were not filled with swirls, which had a negative effect on the communication between zones 1 and 2. Less communication meant less heat transfer between zones 1 and 2. The effect answered the second problem of why internally micro-finned tubes usually have a lower heat-transfer-enhanced ratio at laminar and transition flow regions.

Conflict of interest

The authors declared that there is no conflict of interest.

Acknowledgements

References

[1] R.L. Webb, R. Narayanamurthy, P. Thors, Heat transfer and friction characteristics of internal helical-rib roughness, J. Heat Transf. 122 (2000) 134–142.
[2] W.-T. Ji, A.M. Jacobi, Y.-L. He, W.-Q. Tao, Summary and evaluation on single-phase heat transfer enhancement techniques of liquid laminar and turbulent pipe flow, Int. J. Heat Mass Transf. 88 (2015) 735–754.
[3] X. Liu, M.K. Jensen, Geometry effects on turbulent flow and heat transfer in internally finned tubes, J. Heat Transf. 123 (2001) 1035–1044.
[4] J.B. Copetti, M.H. Macagnan, D. de Souza, R.D.C. Oliveski, Experiments with micro-fin tube in single phase, Int. J. Refrig. 27 (2004) 876–883.

[5] G.J. Zdaniuk, L.M. Chamra, P.J. Mago, Experimental determination of heat transfer and friction in helically-finned tubes, Exp. Therm. Fluid Sci. 32 (2008) 761–775, https://doi.org/10.1016/j.expthermflusci.2007.09.006.

[6] G. Tanda, Effect of rib spacing on heat transfer and friction in a rectangular channel with 45 angled rib turbulators on one/two walls, Int. J. Heat Mass Transf. 54 (2011) 1081–1090.

[7] W.-T. Ji, D.-C. Zhang, Y.-L. He, W.-Q. Tao, Prediction of fully developed turbulent heat transfer of internal helically ribbed tubes – an extension of Gnielinski equation, Int. J. Heat Mass Transf. 55 (2012) 1375–1384.

[8] L. Micheli, K.S. Reddy, T.K. Mallick, General correlations among geometry, orientation and thermal performance of natural convective micro-finned heat sinks, Int. J. Heat Mass Transf. 91 (2015) 711–724.

[9] S. Pirbastami, S.F. Moujaes, S.G. Mol, Computational fluid dynamics simulation of heat enhancement in internally helical grooved tubes, Int. Commun. Heat Mass Transf. 73 (2016) 25–32.

[10] M. Dastmalchi, G.A. Sheikhzadeh, A. Arefmanesh, Optimization of micro-finned tubes in double pipe heat exchangers using particle swarm algorithm, Appl. Therm. Eng. 119 (2017) 1–9.

[11] P. Li, S.J. Eckels, G.W. Mann, N. Zhang, A method of measuring turbulent flow structures with particle image velocimetry and incorporating into boundary conditions of large eddy simulations, J. Fluids Eng. 140 (2018) 071401.

[12] P. Li, S.J. Eckels, G.W. Mann, N. Zhang, Experimental measurements in near-wall regions by particle image velocimetry (PIV), ASME 2014 4th Jt. US-Eur. Fluids Eng. Div. Summer Meet. Collocated ASME 2014 12th Int. Conf. Nanochannels Microchannels Minichannels, American Society of Mechanical Engineers, 2014, V01DT40A004–V01DT40A004.

[13] Z. Dai, D.F. Fletcher, B.S. Haynes, Impact of tortuous geometry on laminar flow heat transfer in microchannels, Int. J. Heat Mass Transf. 83 (2015) 382–398.

[14] Y. Zhai, G. Xia, Z. Chen, Z. Li, Micro-PIV study of flow and the formation of vortex in micro heat sinks with cavities and ribs, Int. J. Heat Mass Transf. 98 (2016) 380–389, https://doi.org/10.1016/j.ijheatmasstransfer.2016.03.044.

[15] C.D. Meinhart, S.T. Wereley, J.G. Santiago, PIV measurements of a microchannel flow, Exp. Fluids. 27 (1999) 414–419, https://doi.org/10.1007/s003480050366.

[16] P. Dupuis, Y. Cormier, M. Fenech, A. Corbeil, B. Jodoin, Flow structure identification and analysis in fin arrays produced by cold spray additive manufacturing, Int. J. Heat Mass Transf. 93 (2016) 301–313.

[17] G. Xia, Z. Chen, L. Cheng, D. Ma, Y. Zhai, Y. Yang, Micro-PIV visualization and numerical simulation of flow and heat transfer in three micro pin-fin heat sinks, Int. J. Therm. Sci. 119 (2017) 9–23.

[18] R.S. Bhatia, R.L. Webb, Numerical study of turbulent flow and heat transfer in micro-fin tubes–part 1, model validation, J. Enhanc. Heat Transf. 8 (2001).

[19] R.S. Bhatia, R.L. Webb, Numerical study of turbulent flow and heat transfer in micro-fin tubes–part 2, parametric study, J. Enhanc. Heat Transf. 8 (2001).

[20] D.N. Ryu, D.H. Choi, V.C. Patel, Analysis of turbulent flow in channels roughened by two-dimensional ribs and three-dimensional blocks–part I: resistance, Int. J. Heat Fluid Flow. 28 (2007) 1098–1111.

[21] D.N. Ryu, D.H. Choi, V.C. Patel, Analysis of turbulent flow in channels roughened by two-dimensional ribs and three-dimensional blocks–part II: heat transfer, Int. J. Heat Fluid Flow. 28 (2007) 1112–1124.

[22] P. Jasiński, Numerical study of friction factor and heat transfer characteristics for single-phase turbulent flow in tubes with helical micro-fins, Arch. Mech. Eng. 59 (2012) 469–485.

[23] R. Campet, M. Zhu, E. Riber, B. Cuenot, M. Nemri, Large eddy simulation of a single-started helically ribbed tube with heat transfer, Int. J. Heat Mass Transf. 132 (2019) 961–969.

[24] ANSYS Fluent Theory Guide, Release 15.0, ANSYS Inc.; 2013.

[25] W.-W. Kim, S. Menon, W.-W. Kim, S. Menon, Application of the localized dynamic subgrid-scale model to turbulent wall-bounded flows 35th Aerosp, Sci. Meet. Exhib. (1997) 210.

[26] P. Li, S.J. Eckels, N. Zhang, G.W. Mann, Effects of parallel processing on large eddy simulations in ANSYS Fluent, ASME 2016 Fluids Eng. Div. Summer Meet. Collocated ASME 2016 Heat Transf. Summer Conf. ASME 2016 14th Int. Conf. Nanochannels Microchannels Minichannels, American Society of Mechanical Engineers, 2016, V01BT26A004–V01BT26A004.

[27] A.R. Betz, D. Attinger, Can segmented flow enhance heat transfer in microchannel heat sinks?, Int J. Heat Mass Transf. 53 (2010) 3683–3691.

[28] C.-Y. Yang, C.-W. Chen, T.-Y. Lin, S.G. Kandlikar, Heat transfer and friction characteristics of air flow in microtubes, Exp. Therm. Fluid Sci. 37 (2012) 12–18.

[29] C.D. Meinhart, S.T. Wereley, M.H.B. Gray, Volume illumination for two-dimensional particle image velocimetry, Meas. Sci. Technol. 11 (2000) 809.

[30] G.W. Mann, S.J. Eckels, Focal plane model for flat refractive geometry, J. Eur. Opt. Soc.-Rapid Publ. 13 (2017) 39.

[31] Insight 4G Software Manual, Revision B., TSI Inc., 2014.

[32] ITTC–Recommended Procedures and Guidelines, Uncertainty Analysis for Particle Imaging Velocimetry (PIV), Visualization Society of Japan, 2011.

[33] J. Pedlosky, Geophysical Fluid Dynamics, Springer Science & Business Media, 2013.

[34] C.K. Batchelor, G.K. Batchelor, An Introduction to Fluid Dynamics, Cambridge University Press, 1967.

[35] R. Courant, K. Friedrichs, H. Lewy, On the partial difference equations of mathematical physics, IBM J. Res. Dev. 11 (1967) 215–234.

[36] G.W. Mann, S. Eckels, Multi-objective heat transfer optimization of 2D helical micro-fins using NSGA-II, Int. J. Heat Mass Transf. 132 (2019) 1250–1261.